Central-Upwind Schemes on Triangular Grids for Hyperbolic Systems of Conservation Laws

Alexander Kurganov,[1] **Guergana Petrova**[2]

[1]*Department of Mathematics, Tulane University, New Orleans, Louisiana 70118*

[2]*Department of Mathematics, Texas A&M University, College Station, Texas 77843*

We present a family of central-upwind schemes on general triangular grids for solving two-dimensional systems of conservation laws. The new schemes enjoy the main advantages of the Godunov-type central schemes—simplicity, universality, and robustness and can be applied to problems with complicated geometries. The "triangular" central-upwind schemes are based on the use of the directional local speeds of propagation and are a generalization of the central-upwind schemes on rectangular grids, recently introduced in Kurganov et al. [SIAM J Sci Comput 23 (2001), 707–740]. We test a second-order version of the proposed scheme on various examples. The main purpose of the numerical experiments is to demonstrate the potential of our method. The more universal "triangular" central-upwind schemes provide the same high accuracy and resolution as the original, "rectangular" ones, and at the same time, they can be used to solve hyperbolic systems of conservation laws on complicated domains, where the implementation of triangular or mixed grids is advantageous. © 2004 Wiley Periodicals, Inc. Numer Methods Partial Differential Eq 21: 536–552, 2005

1. INTRODUCTION

We introduce new central-upwind schemes on general triangular grids for solving the two-dimensional (2-D) system of conservation laws:

$$u_t + f(u)_x + g(u)_y = 0, \tag{1.1}$$

where $u(x, y, t) = (u_1(x, y, t), \ldots, u_N(x, y, t))^T$ and the fluxes are $f = (f_1, \ldots, f_N)^T$ and $g = (g_1, \ldots, g_N)^T$. The schemes belong to the class of Godunov-type central schemes, whose increasing popularity is due to their simplicity, universality, and robustness. Their construction is based on the exact evolution of piecewise polynomial reconstructions of the approximate solution, achieved by integrating (1.1) over Riemann fans. Thus, solving Riemann problems is avoided, and this allows central schemes to be implemented as a "black-box-solver" for a variety of complicated multidimensional systems.

The simplest nonoscillatory central scheme is the first-order (staggered) Lax-Friedrichs scheme [1, 2]. Its second-order generalization was presented in [3] in the one-dimensional (1-D) case and in [4, 5] in two space dimensions. Higher-order extensions have been developed in the past few years in a series of publications: we refer the reader to, for example, [6] and the references therein.

The aforementioned schemes are staggered central schemes. As such, they do not provide high resolution when small time steps (Δt) are enforced, or when long time integration is to be performed. This drawback can be eliminated if local speeds of propagation are used in the estimate of the size of the local Riemann fans. This idea led to the construction of a new family of central schemes [7–9]. They have much smaller numerical dissipation (proportional to Δt) and admit a particularly simple semi-discrete form. The resolution can be increased even more if one-sided local speeds of propagation are used, as demonstrated in [10], where the so-called central-upwind schemes were introduced.

Central-upwind schemes are an excellent tool for solving various complex problems on regular domains. However, in practice one needs to deal with complicated geometries, where using triangular meshes could be advantageous or even unavoidable. With such a grid, it is much easier to adapt cells to the boundary of the domain and to locally perform any adaption strategy without introducing nonconforming nodes (see, e.g., [11]). Staggered central schemes on triangular and tetrahedral grids were developed in [12, 13], but their construction is rather cumbersome, mainly because of staggering.

In contrast to staggered schemes, semi-discrete central schemes can be extended to unstructured grids in a very natural manner. In this article, we present a family of central-upwind schemes on general triangulations, which are simpler than their upwind counterparts, have a genuinely multidimensional structure, and can be used to solve problems on irregular domains. The derivation follows the approach from [8, 10]: we integrate over nonuniform polygonal control volumes of different shapes and derive a fully discrete central-upwind scheme. We then pass to a semi-discrete limit (we let $\Delta t \to 0$, while keeping Δx fixed) and obtain an ODE system for the cell averages of the computed solution of (1.1). The construction of the method is completed by choosing a (stable) ODE solver and a (nonoscillatory) piecewise polynomial reconstruction of appropriate orders.

The article is organized as follows. In §2, we develop our new high-order "triangular" central-upwind schemes. In §3, we test their second-order version on a variety of numerical examples. The second-order scheme uses a piecewise linear interpolant. We have used the piecewise linear reconstruction from [11, 14–16], which we briefly describe in §2.1.

2. NEW CENTRAL-UPWIND SCHEMES ON TRIANGULAR GRIDS: DERIVATION

In this section, we describe the derivation of the new family of central-upwind schemes on triangulations. We assume that a triangulation $\mathcal{T} := \cup T_j$ of the computational domain, consisting of triangular cells T_j of size $|T_j|$, is given. We denote by T_{j1}, T_{j2}, and T_{j3} the
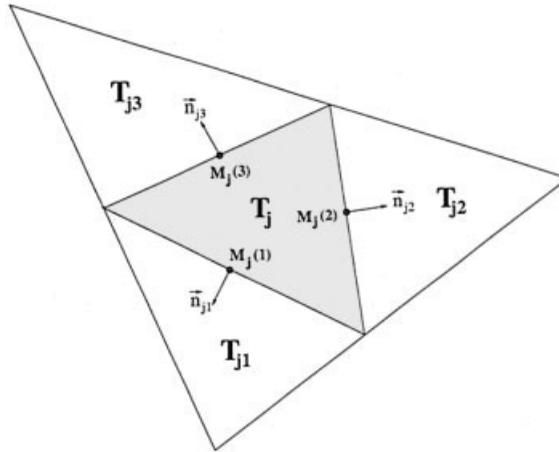
FIG. 1.   Triangular mesh.

neighboring triangles that share a common side with T_j, and by $\vec{n}_{jk} := (\cos(\theta_{jk}), \sin(\theta_{jk}))^T$ the outer unit normals to the corresponding sides of T_j of length h_{jk}, $k = 1, 2, 3$ (Fig. 1).

Our new central-upwind schemes are Godunov-type projection-evolution methods. Their one time step (from $t = t^n := n\Delta t$ to $t = t^{n+1}$) consists of three consecutive stages: reconstruction, evolution, and projection. Next, we provide a detailed description of each of them.

Reconstruction

Suppose that at time $t = t^n$ the cell averages of the computed solution,

$$\bar{u}_j^n \approx \frac{1}{|T_j|} \int_{T_j} u(x, y, t^n) \, dxdy,$$

are available. We then construct a conservative (possibly discontinuous) piecewise polynomial interpolant

$$\tilde{u}^n(x, y) = \sum_j p_j^n(x, y)\chi_j(x, y),$$

where p_j^n is a 2-D polynomial, and χ_j is the characteristic function of T_j. Further, we will denote the value of $\tilde{u}^n$ at a point $G \in T_j$ by

$$u_j^n(G) := p_j^n(G). \tag{2.1}$$

The possible discontinuities of the interpolant $\tilde{u}^n$ along the sides of T_j propagate with different inward, $\{a_{jk}^{\text{in}}\}$, and outward, $\{a_{jk}^{\text{out}}\}$, *directional local speeds*, $k = 1, 2, 3$. They can be estimated, for example, by

$$a_{jk}^{\text{in}} = -\min\{ \min_{M\in T_j\cap T_{jk}} \{\lambda_1[V_{jk}(u_j^n(M))]\}, \min_{M\in T_j\cap T_{jk}} \{\lambda_1[V_{jk}(u_{jk}^n(M)]\}, 0\},$$
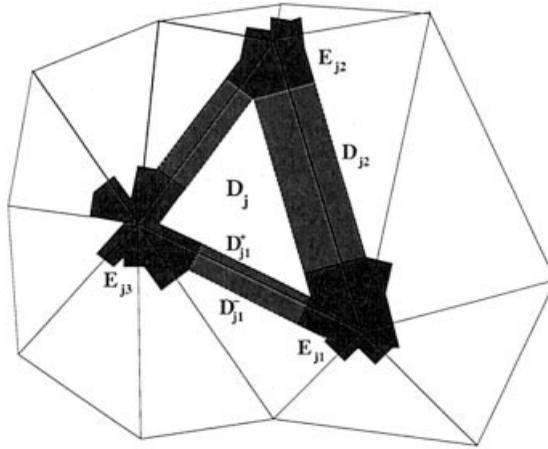
FIG. 2.   Control volumes on a triangulation.

$$a_{jk}^{\text{out}} = \max\{ \max_{M \in T_j \cap T_{jk}} \{\lambda_N[V_{jk}(u_j^n(M))]\}, \max_{M \in T_j \cap T_{jk}} \{\lambda_N[V_{jk}(u_{jk}^n(M)]\}, 0\}, \tag{2.2}$$

where $\lambda_1[V_{jk}] \leq \cdots \leq \lambda_N[V_{jk}]$ are the N eigenvalues of the matrix V_{jk}, defined by

$$V_{jk}(w) = \cos(\theta_{jk}) \frac{\partial f}{\partial u}(w) + \sin(\theta_{jk}) \frac{\partial g}{\partial u}(w).$$

In practice, (2.2) can be often replaced with a simpler estimate:

$$a_{jk}^{\text{in}} = -\min\{\lambda_1[V_{jk}(u_j^n(M_j(k)))], \lambda_1[V_{jk}(u_{jk}^n(M_j(k)))], 0\},$$

$$a_{jk}^{\text{out}} = \max\{\lambda_N[V_{jk}(u_j^n(M_j(k)))], \lambda_N[V_{jk}(u_{jk}^n(M_j(k)))], 0\}, \tag{2.3}$$

where $M_j(k)$ is the midpoint of the kth side of T_j. Note that this estimate may be inaccurate, but the introduced error is comparable with the errors that occur in the computation of the corresponding spatial integrals [see (2.11)], especially when a piecewise linear reconstruction $\tilde{u}^n$ and the second-order midpoint quadrature are used.

The discontinuity along the kth side of T_j can move inward T_j at most by $a_{jk}^{in}\Delta t$, and outward T_j at most by $a_{jk}^{out}\Delta t$. Using this information, we construct the following control volumes: three rectangles D_{jk}, $k = 1, 2, 3$, along each side of T_j, a triangle D_j inside T_j, and three nonconvex domains E_{jk}, $k = 1, 2, 3$, around each vertex of T_j. We denote by D_{jk}^+ and D_{jk}^- the parts of D_{jk} located inside and outside of T_j, respectively. The part of E_{jk} inside T_j is denoted by E_{jk}^+. All these domains are outlined in Fig. 2.

Evolution

Let Q_j be either D_j, D_{jk}, or E_{jk}, $k = 1, 2, 3$. We integrate (1.1) over $Q_j \times [t^n, t^{n+1}]$ to obtain the intermediate cell averages $\bar{w}^{n+1}(Q_j)$ of the computed solution over Q_j at time $t = t^{n+1}$. The computation can be carried out for any particular triangulation along the lines of [8, 10]. To this end, one needs to use appropriate quadratures for the spatial and temporal integrals, which

would only involve those points at the boundary of the control volume, which are located sufficiently far from the discontinuities. This guarantees the smoothness of the solution at these points (for sufficiently small Δt) and helps to avoid solving Riemann problems.

Projection

The computed cell averages over the Q_j's are used for the construction of an intermediate piecewise polynomial function $\tilde{w}^{n+1}$ ($\tilde{w}^{n+1}$ is a polynomial over each of the Q_j's), which is then projected back onto the original triangulation:

$$\bar{u}_j^{n+1} := \frac{1}{|T_j|} \int_{T_j} \tilde{w}^{n+1}(x, y) \, dxdy.$$

This completes the construction of a fully discrete central-upwind scheme on a triangular mesh.

The particular details of this scheme are so messy that the resulting fully discrete scheme becomes impractical. Therefore, we omit these details and proceed within a significantly simpler semi-discrete framework. To this end, we pass to the semi-discrete limit (as $\Delta t \to 0$) in the fully discrete central-upwind scheme. Notice that we will be able to do this without having the explicit form of the fully discrete scheme.

In order to simplify the notation, we now consider the 2-D scalar hyperbolic conservation law:

$$u_t + \vec{\nabla} \cdot \vec{F}(u) = 0, \qquad \vec{F} := (f, g)^T, \qquad \vec{\nabla} := \left(\frac{\partial}{\partial x}, \frac{\partial}{\partial y} \right). \tag{2.4}$$

Systems of conservation laws are treated by complete analogy since no (approximate) Riemann problem solvers are involved.

We begin the derivation of the "triangular" semi-discrete central-upwind schemes by observing that

$$\frac{d}{dt} \bar{u}_j(t^n) = \lim_{\Delta t \to 0} \frac{\bar{u}_j^{n+1} - \bar{u}_j^n}{\Delta t}$$

$$= \lim_{\Delta t \to 0} \frac{1}{\Delta t} \left(\frac{1}{|T_j|} \sum_{k=1}^{3} \int_{D_{jk}^+} \tilde{w}^{n+1} \, dxdy + \frac{1}{|T_j|} \sum_{k=1}^{3} \int_{E_{jk}^+} \tilde{w}^{n+1} \, dxdy + \frac{1}{|T_j|} \int_{D_j} \tilde{w}^{n+1} \, dxdy - \bar{u}_j^n \right). \tag{2.5}$$

The conservation property of $\tilde{w}^{n+1}$ gives

$$\int_{D_j} \tilde{w}^{n+1} \, dxdy = |D_j| \bar{w}^{n+1}(D_j). \tag{2.6}$$

We assume that the spatial derivatives of $\tilde{w}^{n+1}$ are bounded independently of Δt. Then, since by construction $|E_{jk}^+| = \mathbb{O}((\Delta t)^2)$ (Fig. 2) we have

$$\int_{E_{jk}^+} \tilde{w}^{n+1} \, dxdy = \mathbb{O}((\Delta t)^2), \qquad k = 1, 2, 3. \tag{2.7}$$

We also obtain that

$$\int_{D_{jk}^+} \tilde{w}^{n+1} \, dxdy = |D_{jk}^+| \bar{w}^{n+1}(D_{jk}) + \mathbb{O}((\Delta t)^2), \qquad k = 1, 2, 3, \tag{2.8}$$

and therefore from (2.5)–(2.8) we derive

$$\frac{d}{dt} \bar{u}_j(t^n) = \sum_{k=1}^{3} \left(\lim_{\Delta t \to 0} \frac{|D_{jk}^+|}{\Delta t |T_j|} \bar{w}^{n+1}(D_{jk}) \right) + \lim_{\Delta t \to 0} \frac{1}{\Delta t} \left(\frac{|D_j|}{|T_j|} \bar{w}^{n+1}(D_j) - \bar{u}_j^n \right)$$

$$= \frac{1}{|T_j|} \sum_{k=1}^{3} a_{jk}^{\text{in}} h_{jk} \lim_{\Delta t \to 0} \bar{w}^{n+1}(D_{jk}) + \lim_{\Delta t \to 0} \frac{1}{\Delta t} \left(\frac{|D_j|}{|T_j|} \bar{w}^{n+1}(D_j) - \bar{u}_j^n \right). \tag{2.9}$$

The cell averages $\bar{w}^{n+1}(D_{jk})$ are computed by integrating (2.4) over $D_{jk} \times [t^n, t^{n+1}]$ and then by applying Green's theorem:

$$\bar{w}^{n+1}(D_{jk}) = \frac{1}{|D_{jk}|} \left[\int_{D_{jk}^+} p_j^n(x, y) \, dxdy + \int_{D_{jk}^-} p_{jk}^n(x, y) \, dxdy \right] - \frac{1}{|D_{jk}|} \int_{t^n}^{t^{n+1}} \int_{D_{jk}} \text{div} \, \vec{F} \, dxdydt$$

$$= \frac{1}{|D_{jk}|} \left[\int_{D_{jk}^+} p_j^n(x, y) \, dxdy + \int_{D_{jk}^-} p_{jk}^n(x, y) \, dxdy \right] - \frac{1}{|D_{jk}|} \int_{t^n}^{t^{n+1}} \int_{\partial D_{jk}} \vec{F} \cdot \vec{\nu} \, dsdt. \tag{2.10}$$

Here, $\vec{\nu}$ is the outer normal to ∂D_{jk}, which is the boundary of D_{jk}. The spatial integrals in (2.10) are computed using the Gaussian quadrature with m nodes, $x_1, \ldots, x_m$, and weights, $c_1, \ldots, c_m$ ($2m > n$),

$$\int_0^1 \varphi(x) \, dx \approx \sum_{s=1}^{m} c_s \varphi(x_s), \tag{2.11}$$

scaled according to the size of the sides of ∂D_{jk}. Next, from (2.10) and (2.11), and since $|D_{jk}| = \mathbb{O}(\Delta t)$, we obtain

$$\lim_{\Delta t \to 0} \bar{w}^{n+1}(D_{jk}) \approx \frac{1}{a_{jk}^{\text{in}} + a_{jk}^{\text{out}}} \sum_{s=1}^{m} c_s [a_{jk}^{\text{in}} u_j(G_{jk}^s) + a_{jk}^{\text{out}} u_{jk}(G_{jk}^s)]$$

$$- \frac{1}{a_{jk}^{\text{in}} + a_{jk}^{\text{out}}} \sum_{s=1}^{m} c_s [(\vec{F}(u_{jk}(G_{jk}^s)) - \vec{F}(u_j(G_{jk}^s))) \cdot \vec{n}_{jk}], \tag{2.12}$$

where G_{jk}^s, $s = 1, \ldots, m$, are the corresponding scaled Gaussian points on the kth side of T_j.

Similarly to (2.10), we have

$$\bar{w}^{n+1}(D_j) = \frac{1}{|D_j|} \int_{D_j} p_j^n(x, y) \, dxdy - \frac{1}{|D_j|} \int_{t^n}^{t^{n+1}} \int_{\partial D_j} \vec{F} \cdot \vec{n} \, dsdt,$$

with ∂D_j being the boundary of D_j and $\vec{n}$ being $\vec{n}_{jk}$, $k = 1, 2, 3$. Then the last term in (2.9) can be written as

$$\frac{1}{\Delta t} \left(\frac{|D_j|}{|T_j|} \bar{w}^{n+1}(D_j) - \bar{u}_j^n \right) = -\frac{1}{\Delta t |T_j|} \int_{T_j \backslash D_j} p_j^n(x, y) \, dxdy - \frac{1}{\Delta t |T_j|} \int_{t^n}^{t^{n+1}} \int_{\partial D_j} \vec{F} \cdot \vec{n} \, dsdt. \qquad (2.13)$$

Note that $T_j \backslash D_j = D_{j1}^+ \cup D_{j2}^+ \cup D_{j3}^+ \cup E_{j1}^+ \cup E_{j2}^+ \cup E_{j3}^+$, and therefore applying the Gaussian quadrature (2.11) to the spatial integral in (2.13) results in

$$\lim_{\Delta t \to 0} \frac{1}{\Delta t} \left(\frac{|D_j|}{|T_j|} \bar{w}^{n+1}(D_j) - \bar{u}_j^n \right) \approx -\frac{1}{|T_j|} \sum_{k=1}^3 a_{jk}^{in} h_{jk} \sum_{s=1}^m c_s[u_j(G_{jk}^s)]$$

$$-\frac{1}{|T_j|} \sum_{k=1}^3 h_{jk} \sum_{s=1}^m c_s[\vec{F}(u_j(G_{jk}^s)) \cdot \vec{n}_{jk}]. \qquad (2.14)$$

Finally, substituting (2.12) and (2.14) into (2.9) gives the new "triangular" semi-discrete central-upwind scheme:

$$\frac{d\bar{u}_j}{dt} = -\frac{1}{|T_j|} \sum_{k=1}^3 h_{jk} \sum_{s=1}^m c_s \left[\left(\frac{a_{jk}^{in} \vec{F}(u_{jk}(G_{jk}^s)) + a_{jk}^{out} \vec{F}(u_j(G_{jk}^s))}{a_{jk}^{in} + a_{jk}^{out}} \right) \cdot \vec{n}_{jk} \right]$$

$$+ \frac{1}{|T_j|} \sum_{k=1}^3 h_{jk} \sum_{s=1}^m c_s \frac{a_{jk}^{in} a_{jk}^{out}}{a_{jk}^{in} + a_{jk}^{out}} [u_{jk}(G_{jk}^s) - u_j(G_{jk}^s)]. \qquad (2.15)$$

Here, the directional local speeds a_{jk}^{in} and a_{jk}^{out} are defined in (2.3), c_s are the coefficients of the Gaussian quadrature (2.11), G_{jk}^s are the corresponding scaled Gaussian points on the kth side of T_j, and the values of the u's are computed in (2.1), using the piecewise polynomial reconstruction. The CFL-condition, needed to ensure that $D_j \neq \varnothing$, is

$$\Delta t < \min_{i,k} \left[\frac{\ell_{ik}}{3 \max(a_{ik}^{out}, a_{ik}^{in})} \right],$$

where ℓ_{ik}, $k = 1, 2, 3$ are the three corresponding altitudes of triangle $T_i \in \mathcal{T}$.

Remarks. 1. The (formal) spatial order of accuracy of the scheme (2.15), (2.1), (2.3) is determined by the (formal) order of the piecewise polynomial reconstruction $\tilde{u}$ and by the

algebraic degree of precision of the Gaussian quadrature (2.11), that is, by the selection of $\{c_s\}$ and $\{G_{jk}^s\}$. In particular, if we use a second-order piecewise linear reconstruction and the midpoint rule, we end up with the second-order semi-discrete central-upwind scheme on a triangular mesh:

$$\frac{d\bar{u}_j}{dt} = -\frac{1}{|T_j|}\sum_{k=1}^{3} h_{jk}\left(\frac{a_{jk}^{\text{in}}\vec{F}(u_{jk}(M_j(k))) + a_{jk}^{\text{out}}\vec{F}(u_j(M_j(k)))}{a_{jk}^{\text{in}} + a_{jk}^{\text{out}}}\right)\cdot\vec{n}_{jk}$$

$$+ \frac{1}{|T_j|}\sum_{k=1}^{3} h_{jk}\frac{a_{jk}^{\text{in}}a_{jk}^{\text{out}}}{a_{jk}^{\text{in}} + a_{jk}^{\text{out}}}[u_{jk}(M_j(k)) - u_j(M_j(k))]. \qquad (2.16)$$

Here, $M_j(k)$ is the midpoint of the kth side of the triangle T_j, $k = 1, 2, 3$, and $u_j(M_j(k))$ and $u_{jk}(M_j(k))$ are the corresponding values at $M_j(k)$ of the linear pieces over the cells T_j and T_{jk}, respectively.

2. We would like to point out that no (approximate) Riemann solvers have been used in the derivation of the schemes (2.15), (2.1), (2.3). They do not require any information about the eigenstructure of the Jacobians $\partial f/\partial u$ and $\partial g/\partial u$ beyond the CFL-related local speeds a_{jk}^{in} *and* a_{jk}^{out} and thus can be applied to systems componentwise.

3. The central-upwind schemes (2.15), (2.1), (2.3) are constructed on a nonuniform grid and therefore can be implemented for problems with complicated computational domains.

4. The ODE system (2.15) has to be solved numerically by a (stable) ODE solver of an appropriate order. In the numerical examples, we have used the second-order strong stability-preserving (SSP) Runge-Kutta method from [17], known also as the Heun method.

2.1. On Admissible Piecewise Linear Reconstructions

In this section, we describe the piecewise linear reconstruction we have used in our numerical experiments. This reconstruction belongs to the class of so-called admissible piecewise linear reconstructions [11] and was developed in [11, 14–16] in the context of upwind schemes. Other piecewise linear reconstructions over triangulations are also available (see, e.g., [11] and the reference therein), but our experience indicates that in the context of central-upwind schemes, the one presented here demonstrates the best performance among the reconstructions we tested.

We denote by V_{j3} the common vertex for T_j, T_{j1}, and T_{j2} (the notation for V_{j1} and V_{j2} is similar), by $\mathcal{R}_{jk}$, $k = 1, 2, 3$, the set of all triangles in the triangulation $\mathcal{T}$ that share V_{jk} as a common vertex, by N_j and N_{jk} the centers of mass of T_j and T_{jk}, respectively, and by Q_{jk} the intersection of the line segment N_jN_{jk} with the kth side of T_j (Fig. 3).

We assign a value v_{jk} to each vertex V_{jk} of T_j, computed via

$$v_{jk} := \frac{\sum\limits_{\ell:T_\ell\in\mathcal{R}_{jk}} \bar{u}_\ell|T_\ell|}{\sum\limits_{\ell:T_\ell\in\mathcal{R}_{jk}} |T_\ell|}, \qquad k = 1, 2, 3,$$

and denote by ∇S_j the gradient of the plane passing through the three points (V_{jk}, v_{jk}), $k = 1, 2, 3$. We start the reconstruction process with a possibly oscillatory piecewise linear conservative function, which we call a basic reconstruction. Its linear pieces L_j over the triangle T_j are given by
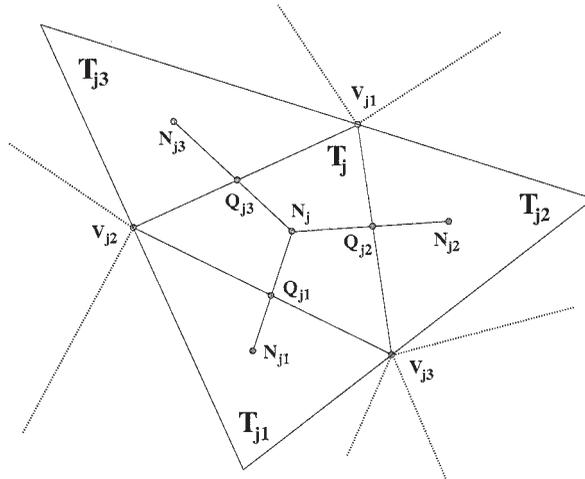
FIG. 3. Admissible reconstruction: floor plan.

$$L_j(\mathbf{x}) = \bar{u}_j + \beta_j \nabla S_j \cdot (\mathbf{x} - \mathbf{x_j}), \qquad \mathbf{x} \in T_j, \qquad T_j \in \mathcal{T}, \tag{2.17}$$

where $\mathbf{x} := (x, y)$, $\mathbf{x_j} := (x_j, y_j)$ are the coordinates of N_j, and $\beta_j = 1$.

Next, we reduce the oscillations present in the basic reconstruction [11, 16], by modifying it to guarantee its admissibility [11, 14] along the line segments $N_j N_{jk}$. The modification is carried out by changing the coefficients β_j in (2.17) and is performed in two steps, (i) and (ii), according to the following algorithm [14].

(i) First, we sweep over all triangles in $\mathcal{T}$ and for each triangle $T_j \in \mathcal{T}$, we check the monotonicity of the values $L_j(Q_{jk})$, $k = 1, 2, 3$, with respect to the corresponding neighboring cell averages $\bar{u}_j$ and $\bar{u}_{jk}$:

- if $L_j(Q_{jk}) < \bar{u}_j < \bar{u}_{jk}$, we change β_j so that the plane (2.17) passes through the point with coordinates $(Q_{jk}, \max\{L_j(Q_{jk}), \bar{u}_j - \alpha\Delta_j\})$.
- if $L_j(Q_{jk}) > \bar{u}_j > \bar{u}_{jk}$, β_j is modified so that the linear function (2.17) passes through $(Q_{jk}, \min\{L_j(Q_{jk}), \bar{u}_j + \alpha\Delta_j\})$.

Here, Δ_j is the diameter of T_j, and α is a free parameter, responsible for the size of the "acceptable" oscillations. Note that the smaller the α, the smaller the oscillations, but at the same time, only taking reasonably large α leads to a uniformly second-order reconstruction. The optimal α depends on the problem at hand. However, our experiments indicate that the numerical solution is not too sensitive to the choice of α. In the numerical examples, presented in §3, we take $\alpha = 0.5$.

(ii) Next, we perform a second sweep over all the triangles and modify the β's only for those triangles T_j, for which the point values $L_j(Q_{jk})$ and $L_{jk}(Q_{jk})$ are between the cell averages $\bar{u}_j$ and $\bar{u}_{jk}$. In this case, we check the monotonicity of the sequence $\bar{u}_j, L_j(Q_{jk}), L_{jk}(Q_{jk}), \bar{u}_{jk}$, and if it is violated, we multiply both β_j and β_{jk} by $\sigma_j^{jk} \in (0, 1)$, so that after the modification $L_j(Q_{jk}) = L_{jk}(Q_{jk})$.

Remark. Note that in both steps (i) and (ii), every slope may be modified more than once, but since after such modifications the linear reconstruction becomes flatter and the sign of β's never
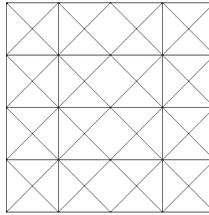
FIG. 4.   Computational domain: triangular mesh.

changes in the process of modification, the local admissibility/monotonicity, once enforced, will never be revoked.

The final reconstruction is then given by (2.17) with the new, modified β_j. The formulae for these β_j's are rather messy and we prefer not to include them.

3. NUMERICAL EXAMPLES

In this section, we present a number of numerical experiments that have been performed using the new second-order "triangular" central-upwind scheme (2.16), (2.1)–(2.3) together with the piecewise linear reconstruction (2.17).

3.1. Square Domain

In the first set of numerical experiments, the computational domain is the square $[0, 1] \times [0, 1]$ with a mesh, schematically shown in Fig. 4. The goal of this experiments is to demonstrate that when using the same number of computational cells, the "triangular" central-upwind schemes provide for problems with a rather complicated wave structures as high resolution as the original "rectangular" schemes. We compare the solutions obtained by the new "triangular" second-order semi-discrete central-upwind scheme with the solutions, computed by the "rectangular" scheme that uses the generalized minmod reconstruction with $\theta = 1.3$ [10, 18]. For fair comparison, we always use the same number of cells—whether triangular or rectangular ones. We also project the final "rectangular" solution onto the corresponding triangular grid and plot it using the same MATLAB procedure as used for plotting the "triangular" solution.

3.1.1. Accuracy Test—2-D Linear Advection Equation.   The "triangular" second-order semi-discrete central-upwind scheme (2.16), (2.1), (2.3), (2.17) is applied to the initial-value problem

$$\begin{cases} u_t + u_x + u_y = 0, \\ u(x, y, 0) = \sin^2(\pi x)\sin^2(\pi y), \end{cases} \tag{3.1}$$

subject to the periodic boundary conditions. We calculate the L^1- and L^∞-errors at time $t = 1$. The results, presented in Table I, clearly indicate the second-order convergence rate.

3.1.2. 1-D Riemann Problem.   We consider the 2-D compressible Euler equations of gas dynamics for ideal gases,

TABLE I.   Accuracy test for the linear advection problem (3.1), $t = 1$.

No. of triangles	L^1-error	Rate	L^∞-error	Rate
$4 \times 25 \times 25$	6.8361×10^{-4}	—	1.5835×10^{-3}	—
$4 \times 50 \times 50$	1.6972×10^{-4}	2.01	3.8585×10^{-4}	2.04
$4 \times 100 \times 100$	4.2346×10^{-5}	2.00	9.5268×10^{-5}	2.02
$4 \times 200 \times 200$	1.0580×10^{-5}	2.00	2.3676×10^{-5}	2.01

$$\frac{\partial}{\partial t}\begin{bmatrix} \rho \\ \rho u \\ \rho v \\ E \end{bmatrix} + \frac{\partial}{\partial x}\begin{bmatrix} \rho u \\ \rho u^2 + p \\ \rho u v \\ u(E + p) \end{bmatrix} + \frac{\partial}{\partial y}\begin{bmatrix} \rho v \\ \rho u v \\ \rho v^2 + p \\ v(E + p) \end{bmatrix} = 0, \qquad p = (\gamma - 1)\left[E - \frac{\rho}{2}(u^2 + v^2)\right],$$

(3.2)

where ρ, u, v, p, and E are the density, the x- and y-velocities, the pressure, and the energy, respectively. In this example, we solve the 1-D Riemann problem, proposed in [19], artificially extended to two space dimensions: the initial data are

$$(p,\, \rho,\, u,\, v)(x,\, y,\, 0) = \begin{cases} (1.0,\, 1.000,\, 0,\, 0), & \text{if } x < 0.5, \\ (0.1,\, 0.125,\, 0,\, 0), & \text{if } x > 0.5. \end{cases}$$

(3.3)

The initial-value problem (3.2)–(3.3) is numerically solved by our new "triangular" central-upwind scheme (2.16), (2.1), (2.3), (2.17) and by its "rectangular" counterpart from [10]. Notice that this 1-D Riemann problem aligns with the rectangular grid, and therefore one expects the "rectangular" scheme to substantially outperform the "triangular" one. However, the computed density profiles, shown from different prospectives in Fig. 5, demonstrate that even though the "triangular" solution is slightly oscillatory, the overall resolution, achieved by both methods, is comparable.

3.1.3. 2-D Riemann Problem.   We numerically solve the 2-D Riemann problem for the Euler equations (3.2), subject to initial data of the general form

$$(p,\, \rho,\, u,\, v)(x,\, y,\, 0) = \begin{cases} (p_1,\, \rho_1,\, u_1,\, v_1), & \text{if } x > 0.5 \text{ and } y > 0.5, \\ (p_2,\, \rho_2,\, u_2,\, v_2), & \text{if } x < 0.5 \text{ and } y > 0.5, \\ (p_3,\, \rho_3,\, u_3,\, v_3), & \text{if } x < 0.5 \text{ and } y < 0.5, \\ (p_4,\, \rho_4,\, u_4,\, v_4), & \text{if } x > 0.5 \text{ and } y < 0.5. \end{cases}$$

(3.4)

It admits 19 genuinely different configurations for polytropic gas [20], distinguished by the three types of 1-D waves between each two neighboring states, namely rarefaction- ($\vec{R}$), shock- ($\vec{S}$) and contact-wave ($\vec{J}$) (consult [20, 21] for details). Here, we have chosen to test our scheme on 3 of the 19 configurations.

Configuration 7

$$\begin{array}{cc} & \overrightarrow{R}_{21} \\ \overleftarrow{J}_{32} & \overrightarrow{R}_{41} \\ & \overleftarrow{J}_{34} \end{array}$$
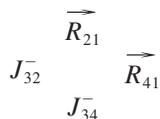
The initial data are as follows:
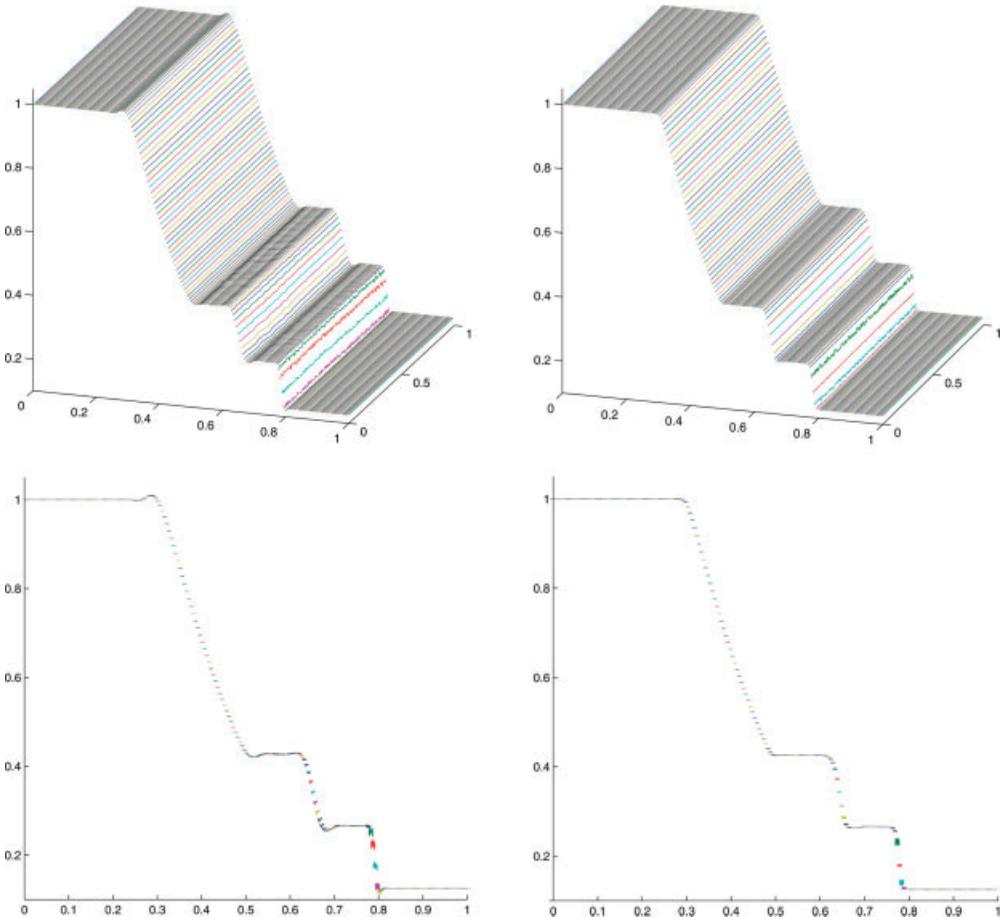
FIG. 5.   Solution of (3.2)–(3.3) by the "triangular" (left) and "rectangular" (right) central-upwind schemes. Density at $t = 0.16$. (Color figure can be viewed in the online issue, which is available at www.interscience.wiley.com.)

$$p_2 = 0.4 \qquad \rho_2 = 0.5197 \quad p_1 = 1 \quad \rho_1 = 1$$
$$u_2 = -0.6259 \quad v_2 = 0.1 \qquad u_1 = 0.1 \quad v_1 = 0.1$$

$$p_3 = 0.4 \quad \rho_3 = 0.8 \quad p_4 = 0.4 \quad \rho_4 = 0.5197$$
$$u_3 = 0.1 \quad v_3 = 0.1 \quad u_4 = 0.1 \quad v_4 = -0.6259$$

Configuration 11

$$\overleftarrow{S_{21}}$$
$$J_{32}^+ \qquad \overleftarrow{S_{41}}$$
$$J_{34}^+$$

The initial data are as follows:
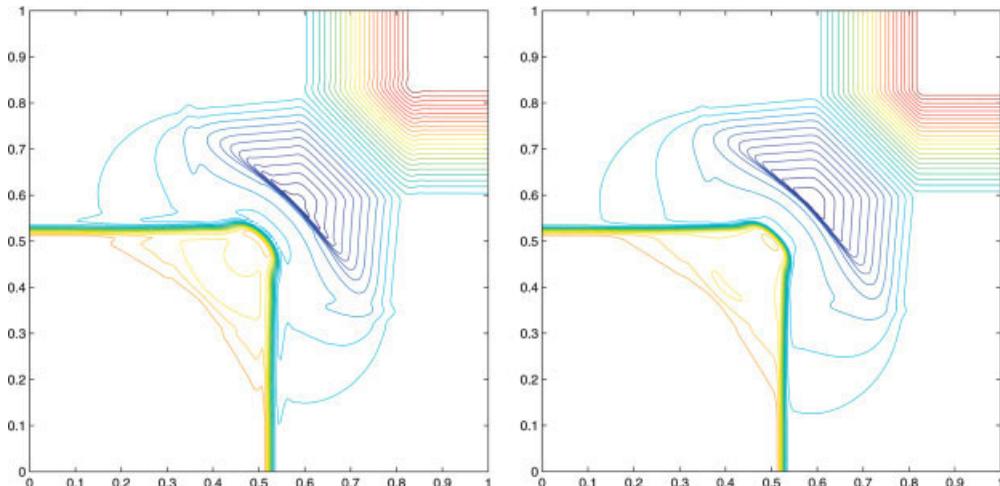
FIG. 6.   Solution of (3.2), (3.4), Configuration 7, by the "triangular" (left) and "rectangular" (right) central-upwind schemes. Density contours at $t = 0.25$. (Color figure can be viewed in the online issue, which is available at www.interscience.wiley.com.)

$$p_2 = 0.4 \qquad \rho_2 = 0.5313 \quad p_1 = 1 \qquad \rho_1 = 1$$
$$u_2 = 0.8276 \quad v_2 = 0 \qquad u_1 = 0.1 \quad v_1 = 0$$

$$p_3 = 0.4 \quad \rho_3 = 0.8 \quad p_4 = 0.4 \quad \rho_4 = 0.5313$$
$$u_3 = 0.1 \quad v_3 = 0 \qquad u_4 = 0.1 \quad v_4 = 0.7276$$

Configuration 12

$$\overset{\longrightarrow}{S_{21}}$$
$$J_{32}^+ \qquad \overset{\longrightarrow}{S_{41}}$$
$$J_{34}^+$$

The initial data are as follows:

$$p_2 = 1 \qquad \rho_2 = 1 \quad p_1 = 0.4 \quad \rho_1 = 0.5313$$
$$u_2 = 0.7276 \quad v_2 = 0 \quad u_1 = 0 \qquad v_1 = 0$$

$$p_3 = 1 \quad \rho_3 = 0.8 \quad p_4 = 1 \quad \rho_4 = 1$$
$$u_3 = 0 \quad v_3 = 0 \qquad u_4 = 0 \quad v_4 = 0.7276$$

We compare the solutions, obtained by our "triangular" scheme (2.16)–(2.17), (2.1)–(2.3) with the ones, obtained by the original "rectangular" central-upwind scheme [18]. The compu- tations are performed on comparable grid sizes—$4 \times 200 \times 200$ triangles for the "triangular" scheme and 400×400 cells for the "rectangular" one. The nonreflecting boundary conditions are obtained by the ghost cell technique.

As one can see in Figs. 6–8, the solution obtained by the "triangular" scheme is slightly more oscillatory, but this result is expected since the reconstruction (2.17) is uniformly second-order and thus more oscillatory then the (formally first-order) minmod reconstruction. Some of the
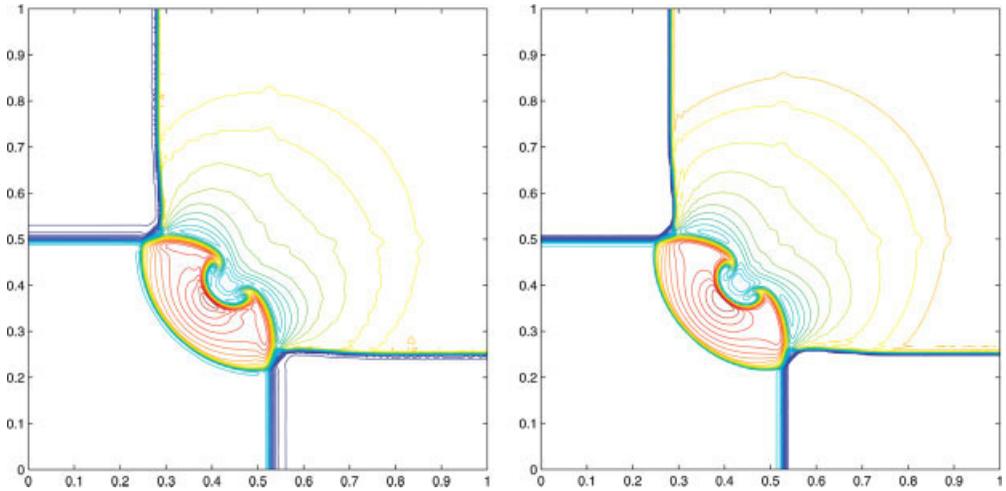
FIG. 7.   Solution of (3.2), (3.4), Configuration 11, by the "triangular" (left) and "rectangular" (right) central-upwind schemes. Density contours at $t = 0.3$. (Color figure can be viewed in the online issue, which is available at www.interscience.wiley.com.)

oscillations can be also interpreted as a natural side effect of the triangular mesh. Notice that the differences in resolution are minor, and overall performance of both schemes is comparable.

3.2. Trapezoidal Domain

In the second set of numerical tests, we show that the new schemes can be applied to solve hyperbolic systems of conservation laws on polygonal domains. Every such domain can be viewed as a union of trapezoids and/or triangles (an example of a polygonal domain split into 10 subdomains is shown in Fig. 9). Thus, for demonstration purposes, we restrict our experi-
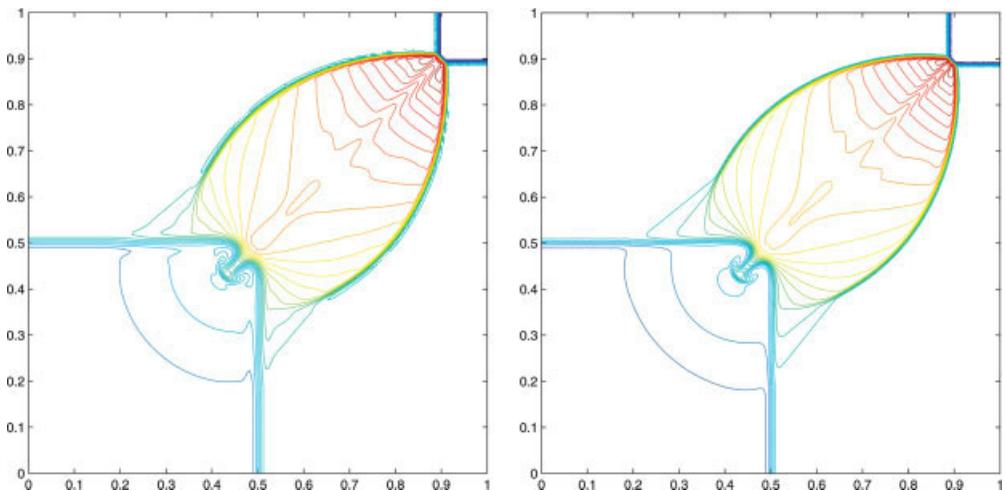
FIG. 8.   Solution of (3.2), (3.4), Configuration 12, by the "triangular" (left) and "rectangular" (right) central-upwind schemes. Density contours at $t = 0.25$. (Color figure can be viewed in the online issue, which is available at www.interscience.wiley.com.)
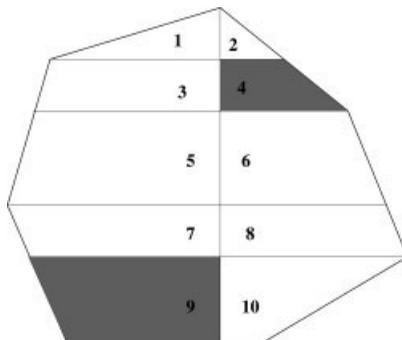
FIG. 9.   A typical polygonal domain.

ments to the case of the trapezoidal domains with a mesh, schematically shown in Fig. 10, where we apply simultaneously the "triangular" central-upwind schemes on the triangular part of the grid and the original "rectangular" schemes on the rectangular cells.

We consider the 2-D Euler equations of gas dynamics, (3.2), for an ideal gas ($\gamma = 1.4$) and numerically solve the problems describing the shock reflection by wedges of different angles. The initial conditions correspond to a right-moving Mach 2 shock, initially positioned at $x = -0.7a$, where a, b, c, d are the lengths of the sides of the trapezoidal computational domain outlined in Fig. 10. The initial shock propagates to the right and then is reflected by the solid wedge.

Contour plots of the density are presented in Fig. 11. We consider different wedge angles θ that correspond to the following four sets of data:

- Figure 11(a): $a = 4$, $b = 34$, $c = 10$, $d = 10\sqrt{10}$, final time $t = 7$;
- Figure 11(b): $a = 3$, $b = 23$, $c = 10$, $d = 10\sqrt{3}$, final time $t = 5$;
- Figure 11(c): $a = 3$, $b = 13$, $c = 10$, $d = 10\sqrt{2}$, final time $t = 3$;
- Figure 11(d): $a = 3$, $b = 4$, $c = 10$, $d = \sqrt{101}$, final time $t = 1.4$.

In all the tests, we have used 400 rectangular computational cells along the lower side of the trapezoid and 400 triangular cells along its right side. The boundary conditions along the lower and right parts of the boundary are treated as a solid wall via the ghost cell technique.
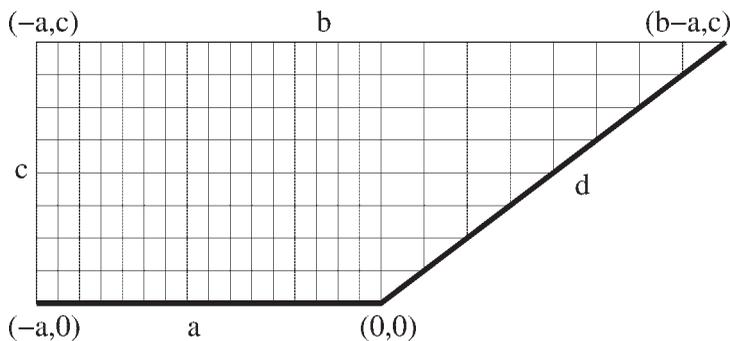
FIG. 10.   Computational domain: mixed rectangular-triangular mesh.
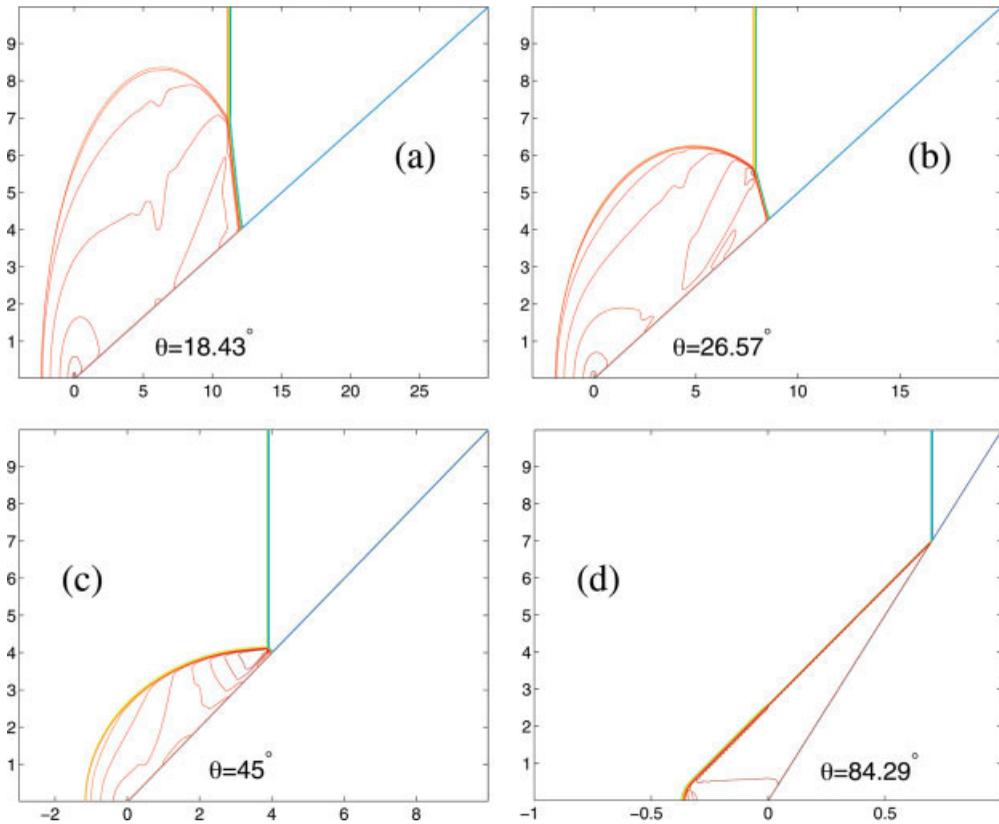
FIG. 11.   Shock reflection by wedges of different angles; density contours. (Color figure can be viewed in the online issue, which is available at www.interscience.wiley.com.)

Remark.   It is well-known that the shock reflection problem, computed in this example, can be reformulated so that the computational domain will become rectangular. However, this technique will obviously fail in the case of a more complicated polygonal domain and/or initial conditions, while our method will still apply.

4. CONCLUDING COMMENTS

The main purpose of this article is to develop semi-discrete central-upwind schemes on general triangulations and to illustrate their potential. Our numerical experiments suggest that these schemes have the same resolution (except maybe slight oscillations due to the triangular mesh) as the central-upwind schemes on rectangular grids. At the same time, they have the essential advantage that they can be applied to problems with complex geometries, where the use of triangular or mixed rectangular-triangular grids is favorable.

References

 1. K. O. Friedrichs, Symmetric hyperbolic linear differential equations, Comm Pure Appl Math 7 (1954), 345–392.

 2. P. D. Lax, Weak solutions of nonlinear hyperbolic equations and their numerical computation, Comm Pure Appl Math 7 (1954), 159–193.

 3. H. Nessyahu and E. Tadmor, Non-oscillatory central differencing for hyperbolic conservation laws, J Comput Phys 87 (1990), 408–463.

 4. P. Arminjon and M.-C. Viallon, Généralisation du schéma de Nessyahu-Tadmor pour une équation hyperbolique à deux dimensions d'espace, CR Acad Sci Paris t. 320, série I (1995), 85–88.

 5. G.-S. Jiang and E. Tadmor, Non-oscillatory central schemes for multidimensional hyperbolic conservation laws, SIAM J Sci Comput 19 (1998), 1892–1917.

 6. D. Levy, G. Puppo, and G. Russo, A fourth-order central WENO scheme for multidimensional hyperbolic systems of conservation laws, SIAM J Sci Comput 24 (2002), 480–506.

 7. A. Kurganov and D. Levy, A third-order semi-discrete central scheme for conservation laws and convection-diffusion equations, SIAM J Sci Comput 22 (2000), 1461–1488.

 8. A. Kurganov and G. Petrova, A third-order semi-discrete genuinely multidimensional central scheme for hyperbolic conservation laws and related problems, Numer Math 88 (2001), 683–729.

 9. A. Kurganov and E. Tadmor, New high-resolution central schemes for nonlinear conservation laws and convection-diffusion equations, J Comput Phys 160 (2000), 241–282.

10. A. Kurganov, S. Noelle, and G. Petrova, Semi-discrete central-upwind scheme for hyperbolic conservation laws and Hamilton-Jacobi equations, SIAM J Sci Comput 23 (2001), 707–740.

11. D. Kröner, Numerical schemes for conservation laws, Wiley, Chichester, 1997.

12. P. Arminjon and A. St-Cyr, Nessyahu-Tadmor-type central finite volume methods without predictor for 3D Cartesian and unstructured tetrahedral grids, Appl Numer Math 46 (2003), 135–155.

13. P. Arminjon, M.-C. Viallon, and A. Madrane, A finite volume extension of the Lax-Friedrichs and Nessyahu-Tadmor schemes for conservation laws on unstructured grids, Int J Comput Fluid Dyn 9 (1997), 1–22.

14. M. Ohlberger, private communications.

15. M. Wierse, Solving the compressible Euler equations in timedependent geometries, Proc 5th International Conference on Hyperbolic Problems, Stony Brook, 1994.

16. M. Wierse, Higher-order upwind schemes on unstructured grids for the compressible Euler equations in timedependent geometries in 3-D, PhD Thesis, University of Freiburg, 1994.

17. S. Gottlieb, C.-W. Shu, and E. Tadmor, Strong stability-preserving high order time discretization methods, SIAM Rev 43 (2001), 89–112.

18. A. Kurganov and E. Tadmor, Solution of two-dimensional Riemann problems for gas dynamics without Riemann problem solvers, Numer Methods Partial Differential Eq 18 (2002), 584–608.

19. G. Sod, A survey of several finite different methods for systems of nonlinear hyperbolic conservation laws, J Comput Phys 22 (1978), 1–31.

20. C. W. Schulz-Rinne, J. P. Collins, and H. M. Glaz, Numerical solution of the Riemann problem for two-dimensional gas dynamics, SIAM J Sci Comput 14 (1993), 1394–1414.

21. C. W. Schulz-Rinne, Classification of the Riemann problem for two-dimensional gas dynamics, SIAM J Math Anal 24 (1993), 76–88.